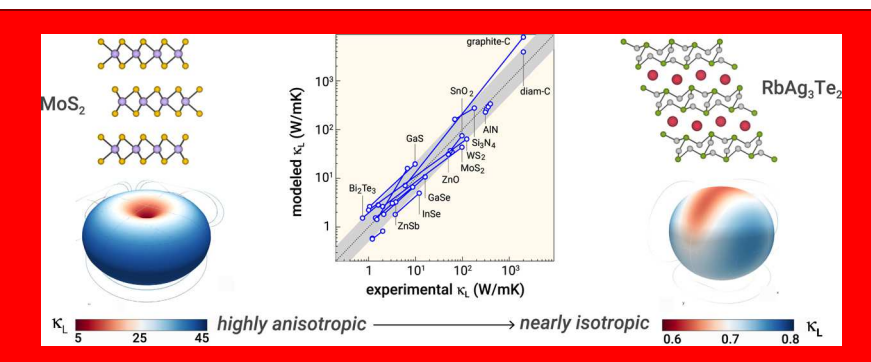


Rapid Prediction of Anisotropic Lattice Thermal Conductivity: **Application to Layered Materials**

Robert McKinney, ** Prashun Gorai, ** Eric S. Toberer, ** and Vladan Stevanovič**, **

[†]Physics and [‡]Metallurgical and Materials Engineering, Colorado School of Mines, Golden, Colorado 80401-1887, United States

Supporting Information



Thermal conductivity plays a crucial role in many applications; the use of single-crystal and textured polycrystalline materials in such applications necessitates understanding the anisotropy in thermal transport. The measurement of anisotropic lattice thermal conductivity $\kappa_1(\theta,\phi)$ is quite challenging. To address this need through computations, we build upon our previously developed isotropic model for κ_L and incorporate the directional (angular) dependence by using the elastic tensor obtained from ab initio calculations and the Christoffel equations for the speed of sound. With the anisotropic speed of sound and intrinsic material properties as input parameters, we can predict the direction-dependent $\kappa_{\rm L}(\theta,\phi)$. We validate this new model by comparing with the experimental data from the literature—the predicted κ_L is within an average factor difference of 1.8 of experimental measurements, spanning 5 orders of magnitude in κ_L . To demonstrate the utility and computational tractability of this model, we calculate $\kappa_L(\theta,\phi)$ of ~2200 layered materials that are expected to exhibit anisotropic thermal transport. We consider both van der Waals and ionic layered structures with binary and ternary chemistries and analyze the anisotropy in their κ_1 . The large-scale study has revealed many layered structures with interesting anisotropy in κ_1 .

■ INTRODUCTION

In applications such as thermoelectrics and power electronics, the lattice thermal conductivity (κ_L) plays a critical role in the material's performance. 1-8 Although materials with high thermal conductivity are desirable for power electronic and solid-state lighting, low-thermal-conductivity materials are attractive for thermoelectrics and thermal-barrier coatings. Methods to both enhance and suppress thermal conductivity of materials have been extensively explored. 9-11 Examples include single-crystal growth 12 and synthesis of low-dimensional structures¹³ for high thermal conductivity and nanostructuring¹⁴ and alloying¹⁵ for low thermal conductivity.

In the computationally driven searches for novel materials with high or low thermal conductivity, calculations typically fall within one of the two approaches: (1) direct ab initio calculations of phonon-phonon scattering rates and associated relaxation times, followed by solving the Boltzmann transport equation for phonons^{16–19} or (2) high-throughput computations which utilize semiempirical or statistical-learning models. 10,20 Ab initio calculations of thermal conductivity which go beyond the relaxation time approximation must account for all sources of phonon scattering to solve the Boltzmann transport equation for phonons. 21-28 Historically,

the complexity of such calculations has limited computations to only a handful of materials at a time. Although computational efficiency has improved to the point where such methods can now be applied to larger number of materials, the prediction accuracy is still on the order of 50%.^{3,10} In contrast, high-throughput methods reduce computational complexity by utilizing experimental data and employing assumptions about scattering to rapidly screen large databases of materials for desired properties. 1,3,4,10,20,29-32 A common tool in high-throughput computation, semiempirical models maintain the overall physical relationships while using experimental data to find best fit solutions. The advantage of semiempirical models is that they can often achieve near the same level of accuracy as ab initio models at a fraction of the computational cost, making them more suitable to highthroughput screening.

The materials science community has been increasingly interested in single crystals and textured polycrystalline materials with anisotropic transport. For instance, in thermo-

Received: December 10, 2018 Revised: February 12, 2019 Published: February 15, 2019



electrics, even though materials are typically synthesized as bulk polycrystalline samples (where transport anisotropy is averaged out), anisotropy in grain orientations and in electronic and phonon transport has been shown to enhance thermoelectric performance. [14,27,33,34] Moreover, materials that are inherently anisotropic, such as 2D materials created by exfoliation of bulk-layered materials, have demonstrated remarkable properties and utility in thin-film applications. [35–42]

Many compounds, particularly those with layered structures, are known to exhibit large anisotropy in thermal conductivity, for example, in-plane versus out-of-place for layered structures. $^{12,28,43-56}$ Transition metal dichalcogenides such as MoS $_2$ and WS $_2$ have in-plane and out-of-plane $\kappa_{\rm L}$ that differ by more than an order of magnitude. 56,57 SnSe, one of the highest zT thermoelectric materials, has an extremely low overall thermal conductivity, but because of the layered structure exhibits, $\kappa_{\rm L}\approx 1.5\times$ lower in the out-of-plane direction compared to that in the in-plane direction. 26,58,59 We show experimentally measured values of anisotropic lattice thermal conductivity from the literature in Figure 1, which highlights the range of $\kappa_{\rm L}$ anisotropy in materials. $^{12,28,43-56}$

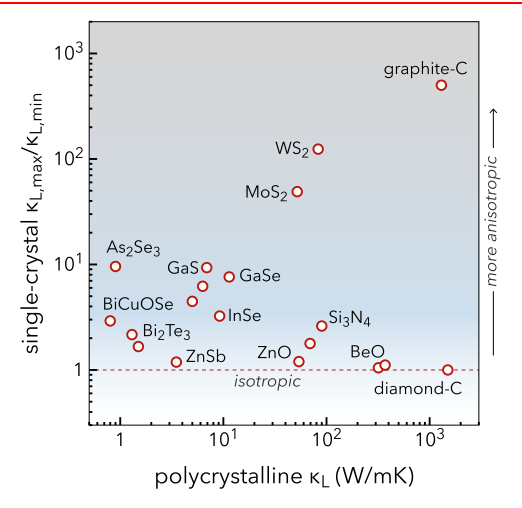


Figure 1. Compilation of measured $^{12,43-55}$ and calculated (As₂Se₃, BiCuOSe) 28,56 anisotropic lattice thermal conductivity (κ_L) from the literature. The ratio of maximum to minimum κ_L in single crystals is plotted against the measured value in polycrystalline samples to demonstrate the large anisotropy in κ_L of certain materials.

The data in Figure 1 emphasize the need to consider anisotropy in a lattice thermal conductivity model to properly account for directional variation of $\kappa_{\rm L}$ in materials such as MoS₂, WS₂, and graphite. S5,60 The direct calculation of anisotropic $\kappa_{\rm L}$ is possible with ab initio methods for computing phonon—phonon scattering relaxation times. However, such methods are not amenable to high-throughput computation of large material sets. There exists a need for a simple, computationally tractable model to predict the direction-dependent $\kappa_{\rm L}$ that can be applied in high-throughput assessment of a large number of materials.

We have previously developed a semiempirical, *isotropic* model for κ_L ; the predictive power of this model is on par with accurate but computationally expensive ab initio methods. Although still useful, the isotropic, semiempirical model does not provide the detailed direction-dependent κ_L that is needed to understand the thermal transport in anisotropic materials. Herein, we expand upon this semi-

empirical model to incorporate anisotropy. By replacing the isotropic estimation of the speed of sound in the prior model with a directionally variant speed of sound $v_s(\theta,\phi)$, we predict the direction-dependent $\kappa_L(\theta,\phi)$. We determine $v_s(\theta,\phi)$ from the elastic stiffness tensor (C_{ij}) by utilizing the Christoffel equations $^{61-65}$ —a set of equations for computing the longitudinal and the two transverse-mode speeds of sound along any unit vector. The elastic tensor can be straightforwardly calculated with first-principles density functional theory (DFT) methods. Although the computational expense to evaluate the new direction-dependent model is only moderately higher compared to the previous isotropic model, it is still significantly lower than direct ab initio models.

We have validated the new model for $\kappa_L(\theta,\phi)$ by comparing the predicted values to experimental measurements; the model predicts κ_L within an average factor difference of 1.8 across 4–5 orders of magnitude. Using this model, we predict the directionally dependent κ_L of 2261-layered materials, including van der Waals (vdW)- and ionic-layered structures, which we had previously identified in another study. We show that vdW-layered materials are generally more anisotropic than ionic-layered materials because of their structural differences in interlayer bonding. We investigate several case examples to understand the driving factors that govern the magnitude and anisotropy of phonon transport in these materials.

■ LATTICE THERMAL CONDUCTIVITY MODELS

Prior Work: Direction-Agnostic κ_L **Model.** For high-throughput prediction of κ_L , we have previously developed and iterated upon a simple model that approximates phonon scattering and speed of sound and which reproduces measured values of κ_L to within a factor of two. 4,30,68 This model was based on the quasiclassical, Boltzmann transport theory for phonons, which results in the following expression for the lattice thermal conductivity 33,68

$$\kappa_{\rm L} = \frac{1}{3} \int_0^{\omega_{\rm max}} C_{\nu}(\omega) v_{\rm g}(\omega)^2 \tau(\omega) \, d\omega \tag{1}$$

Our previous model treats acoustic and optical phonon contributions separately because there is a fundamental difference in group velocity between the two. The acoustic phonon contribution to κ_L is calculated using the Callaway model by assuming the high-temperature limit for the Debye heat capacity, Umklapp scattering as the dominant scattering mechanism, and approximating the group velocity with the speed of sound. The integration is carried out to a maximum frequency, $\omega_{\rm a}=\omega_{\rm D}/N^{1/3}\overset{4,33,68}{.}$ In complex materials with many atoms per cell, most of the heat is carried in the optical phonons. The lower bound to heat transported by optical phonons can be found by assuming a glasslike relaxation time, $\tau_{\rm glass} = \pi/\omega$, and integrating the Callaway model from a minimum frequency, $\omega_{
m D}/N^{1/3}$, again assuming the hightemperature limit to the heat capacity.⁶⁸ Combining the acoustic and optical phonon contributions yields a semiempirical model for κ_L which combines quantities that can be obtained from DFT with parameters fit to yield the smallest error with experimental values.

$$\begin{split} \kappa_{\rm L_{ac}}^{\rm iso} &= A_1 \frac{\overline{M} \nu_{\rm s}^{y}}{T \gamma^2 V^Z n^x} \\ \kappa_{\rm L_{op}}^{\rm iso} &= \frac{3k_{\rm B}}{2} \left(\frac{\pi}{6}\right)^{1/3} \frac{\nu_{\rm s}}{V^z} \left(1 - \frac{1}{n^{2/3}}\right) \\ \kappa_{\rm L_{tot}}^{\rm iso} &= \kappa_{\rm L_{ac}}^{\rm iso} + \kappa_{\rm L_{op}}^{\rm iso} \end{split} \tag{2}$$

The prefactor A_1 and the exponents x, y, and z were fit using experimental data and have the values: $A_1 = 0.00269$, x =1.04778, y = 4.43483, and z = 0.33485. \overline{M} is the average atomic mass, v_s is the speed of sound, V is the average volume per atom, γ is the Grüneisen parameter, and n is the number of atoms in the primitive cell. All of the parameters, except for the speed of sound and Grüneisen parameter, are easily obtained from structural data associated with the compound. The isotropic speed of sound is approximated from the bulk modulus and the density, $v_{\rm s} \approx \sqrt{\frac{B}{d}}$. The bulk modulus can be calculated using the Birch-Murnaghan equation of state⁶⁹ fitted to the energy-volume dependence computed using DFT or some other total energy method.³⁰ Miller et al. found a semiempirical relation for the Grüneisen parameter which depends on the average coordination number per atom (CN) within a material, suggesting that as the atoms become more coordinated, the anharmonicity of the material increases, as shown in eq 3.4 The Grüneisen fit parameters ($\gamma_0 = 7.33688$, a = 0.05868, and $CN_0 = 2.13647$) were found by fitting measured Grüneisen parameters to calculate the average coordination numbers. We leave this equation unaltered for most materials, except in cases of very low coordination number (see section: Direction-Dependent κ_L Model).

$$\gamma = \gamma_0 (1 - e^{-a(\text{CN} - \text{CN}_0)}) \tag{3}$$

The previous model of κ_L has been shown to have an average factor difference less than 2 across four orders of magnitude and has proven highly amenable to the high-throughput search for directionally agnostic κ_L . 1,4,30

Direction-Dependent Speed of Sound. To describe the lattice thermal conductivity of anisotropic materials and account for the directional dependence of κ_L , we modify our previous model by replacing the isotropic speed of sound with an anisotropic quantity. We choose to replace only the speed of sound for three reasons: (a) because the exponent on the speed of sound term is 4.43 in the acoustic component, small variations in the absolute value will be magnified more than any other component; (b) the components \overline{M} , V, and n do not have a directional component; (c) although γ can be anisotropic, the range of values is fairly restricted when compared to the possible range of speed of sound, and the exponent is much smaller than the speed of sound exponent in the acoustic term.

A direction-dependent speed of sound can be calculated from the elastic tensor, C, using the Christoffel eigenvalue equation, as shown in eq $4.6^{61,62,70-73}$

$$\sum_{ijkl} |\rho v^2(\vec{n}) \delta_{ij} - C_{ijkl} n_k n_l| = 0$$
(4)

Here, ρ is the density of the material, $v(\vec{n})$ is the magnitude of the speed of sound for a particular mode along the unit vector \vec{n} , C_{ijkl} is a component of the rank-4 elastic tensor, and n_k and n_l are components of the unit vector corresponding to the

direction of propagation.⁷⁴ In this equation, the eigenvalues are the squares of the three values of speed of sound and the corresponding eigenvectors are the three polarizations: one longitudinal and two transverse.

Given the elastic tensor and the density of a material, we can calculate three modes of speed of sound for every direction by varying the propagation vector and resolving eq 4. We demonstrate this in Figure 2 for three test materials: Bi₂Te₃,

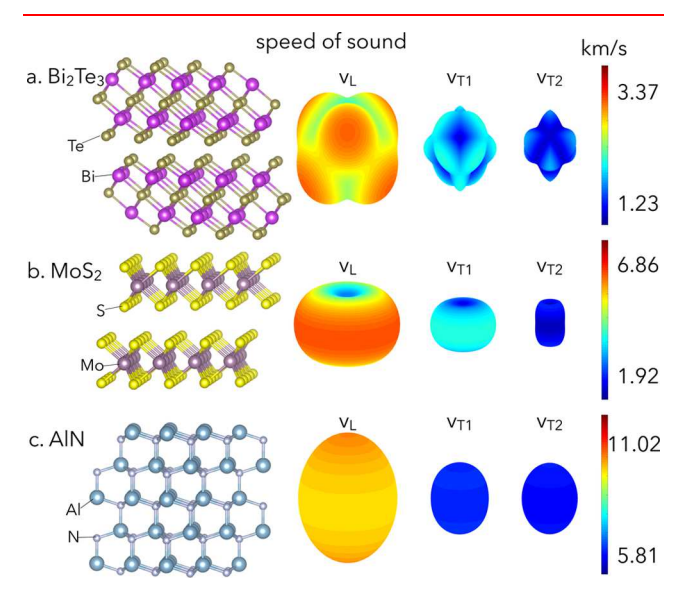


Figure 2. Polar plots of the calculated longitudinal (ν_L) and two transverse-mode (ν_{T1}, ν_{T2}) speeds of sound for (a) Bi_2Te_3 , (b) MoS_2 , and (c) AlN. The radius and color both represent the value of ν in km/s. The minimum and maximum ν for each material are labeled next to the colorbar.

MoS₂, and AlN. In this figure, we show the three modes of the speed of sound calculated as a function of polar angles: $v_{\rm L}(\theta,\phi), \, v_{\rm T1}(\theta,\phi)$, and $v_{\rm T2}(\theta,\phi)$. The color and radius of each plot correspond to the magnitude along a particular lattice vector. Speeds of sound in these plots are calculated using experimental values of the room-temperature elastic tensor components (C_{ij}) and densities taken from the literature.

The speed of sound varies depending on the anisotropy of the crystal structure. Bi₂Te₃, a well-known thermoelectric which is vdW-layered, shows peaks in the longitudinal mode along the directions corresponding to the stretching of chemical bonds, which are expected to be directions of high stiffness, as shown in Figure 2a. MoS2, a hexagonal vdWlayered structure, has a longitudinal mode that varies by nearly a factor of 4 between waves directed within the plane of the layers and waves directed across the layers, as shown in Figure 2b. The hexagonal lattice leads to invariant in-plane speed of sound in all three modes. In the wurtzite AlN, the polar plots are nearly spherical, as shown in Figure 2c. There is a slight distortion along the c-axis in the longitudinal mode which corresponds to the direction of maximum stiffness where bonds align and bond lengths are stretched and compressed rather than rotated. In all three structures, the two transverse modes have magnitudes which are nearly a factor of 2 smaller than the longitudinal mode.

Direction-Dependent κ_L **Model.** Given the angular speed of sound, we can now calculate the angular lattice thermal conductivity by replacing the isotropic speed of sound in the original model (eq 2) without changing other parameters to

preserve the accuracy of the isotropic magnitude while allowing the directional value to vary with the speed of sound. Because each mode contributes separately to the total lattice thermal conductivity, $\kappa_L(\theta,\phi)$ is computed as an average of the three modes for any direction (θ,ϕ) , and hence the overall division by 3 between eq 2 and 5.

$$\begin{split} \kappa_{\mathrm{L}_{\mathrm{ac}}(\theta,\phi)} &= \frac{A_{\mathrm{l}}}{3} \frac{\overline{M}(\nu_{\mathrm{L}}(\theta,\phi)^{y} + \nu_{\mathrm{Tl}}(\theta,\phi)^{y} + \nu_{\mathrm{T2}}(\theta,\phi)^{y})}{T\gamma^{2}V^{z}n^{x}} \\ \kappa_{\mathrm{L}_{\mathrm{op}}(\theta,\phi)} &= \frac{k_{\mathrm{B}}}{2} \bigg(\frac{\pi}{6} \bigg)^{1/3} \frac{(\nu_{\mathrm{L}}(\theta,\phi) + \nu_{\mathrm{Tl}}(\theta,\phi) + \nu_{\mathrm{T2}}(\theta,\phi))}{V^{z}} \\ &\qquad \qquad \bigg(1 - \frac{1}{n^{2/3}} \bigg) \\ \kappa_{\mathrm{L}_{\mathrm{tot}}(\theta,\phi)} &= \kappa_{\mathrm{L}_{\mathrm{ac}}(\theta,\phi)} + \kappa_{\mathrm{L}_{\mathrm{op}}(\theta,\phi)} \end{split} \tag{5}$$

The only other change that we make to the model is to put a floor on the calculated Grüneisen parameter (eq 3) of 0.5. The reason for this is that the semiempirical model for the Grüneisen parameter was created using experimental Grüneisen data which ranged from 0.5 to 2.0, with corresponding average CN ranging from 3 to 6.4 The model is known to underestimate Grüneisen parameter for low coordination numbers, which occur frequently among highly anisotropic vdW-layered compounds where average CN is less than 3. Using the same Grüneisen model for such low coordination numbers can lead to unphysical results such as Grüneisen parameters very close to zero, resulting in nearly harmonic systems, or negative, which is unphysical. Because the semiempirical Grüneisen model has proven useful as a feature in the previous model by differentiating systems of similar density and volume which had different levels of average coordination, we wished to leave eq 3 mostly unchanged. Rather than refitting the model for all materials, applying a lower bound to systems with very low average coordination was the more appropriate choice. Because measured values of the Grüneisen parameter fall within the range of 0.5-2.0 (the Grüneisen parameter for graphite is near 0.9), 78 our choice of lower bound is justifiable. By using a hard lower bound for the Grüneisen parameter, the calculated $\kappa_{\rm I}$ for any material where this correction is necessary will be reduced because of the γ^{-2} dependence. We expect that this will affect the prediction of vdW-layered materials with very low coordination numbers and subsequently high in-plane κ_L , where the previously predicted Grüneisen parameter would have been unphysically low.

Validation of Anisotropic $\kappa_{\rm L}$ **Model.** Although anisotropic lattice thermal conductivity is not a common measurement, experimental data for various compounds exist in literature. To compare our anisotropic model to experimental values, we calculate the directional $\kappa_{\rm L}$ along reported directions (a, b, or c) to judge the validity of this approach. The volume, average mass per atom, number of atoms per cell, and average coordination number can be found from the reported structures within the inorganic crystal structure database (ICSD). Elastic tensors are calculated from the stress—strain relationship with DFT (see Methods section). For those test compounds which were vdW-layered, we used vdW-corrected functionals in the DFT calculation (denoted in the Supporting Information). As the fitting of the old (isotropic) model is done using room-temperature data,

our new (direction-informed) model also implicitly assumes room-temperature conditions (see Figure 3).

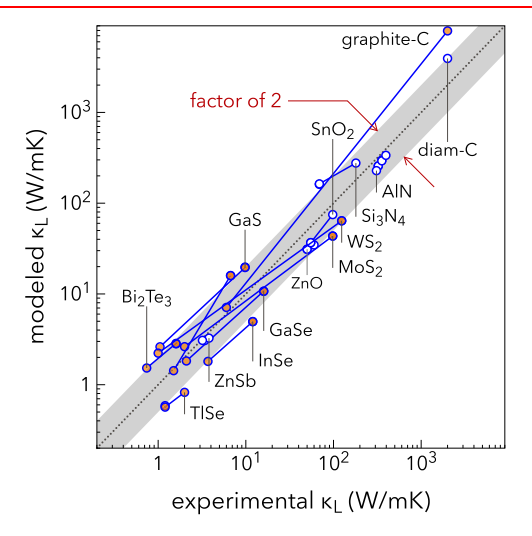


Figure 3. Comparison of modeled κ_L to experimental values. Each material is denoted by a pair of markers, representing the minimum and maximum κ_L , connected by a blue line. The boundary of the greyshaded region represents a factor of 2 error in prediction. Overall, the average factor difference between predicted and experimental κ_L is ~ 1.8 . Orange-filled points correspond to vdW-layered materials.

The most striking result is that all of the connecting lines between $\kappa_{L,max}$ and $\kappa_{L,min}$ in Figure 4 accurately capture the

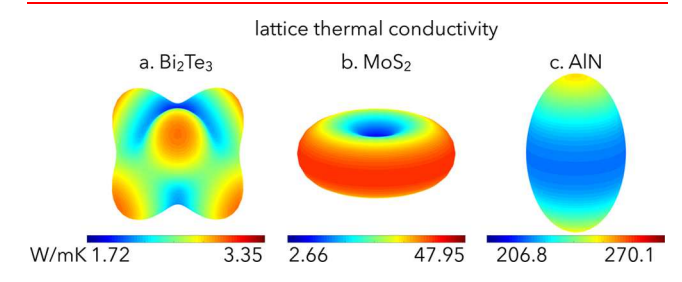


Figure 4. Polar plots of calculated κ_L of (a) Bi₂Te₃, (b) MoS₂, and (c) AlN. The radius and color both represent the value of κ_L in W/m K. The minimum and maximum κ_L for each material is labeled next to the colorbar.

variation. The average error in the slopes on the log plot is a factor difference of 1.5 from unity. This confirms that our model accurately captures the directional variation in κ_{L} and that the thermal transport of materials with $\kappa_{L,max}/\kappa_{L,min} > 1.5$ can be accurately classified as anisotropic rather than isotropic. The second key result is that by only replacing the isotropic speed of sound with an anisotropic value, we are still able to accurately reproduce experimental values from literature within an average factor difference of 1.8. The largest factor difference that we found within the test materials was the in-plane (x and y) value of graphite with an overpredicted value which is nearly a factor of 4 greater than experimental values. It should be noted that although the experimental in-plane value of graphite is on the order of 2000 W/m K, theoretical values for singlecrystal graphite have been reported well above 10 000 W/m K_{\cdot}^{60} The smallest error was in the out-of-plane (z) value of SnSe₂ with a factor difference of 1.05. This anisotropic model works across four orders of magnitude and, importantly,

correctly predicts the direction, if not the magnitude, of the variation between $\kappa_{\rm L,min}$ and $\kappa_{\rm L,max}$ for all materials.

In Figure 4, we show the lattice thermal conductivity in all directions for the three test materials from Figure 2. What is immediately apparent when comparing Figures 2 and 4 is that the longitudinal mode dominates the lattice thermal conductivity. This occurs because the longitudinal mode has a higher magnitude than transverse modes, which is then enhanced in the lattice thermal conductivity because of the exponent, y, on the acoustic component. The dominating features in the longitudinal mode of the speed of sound plots are exaggerated in the plots of $\kappa_{\rm L}$, showing that thermal transport occurs best along directions corresponding to stretching of bond lengths. This point is also highlighted when comparing different materials. The difference in $\nu_{\rm L}$ between Bi₂Te₃ and AlN is only about a factor 3, but this translates to over two orders of magnitude of difference in $\kappa_{\rm L}$.

APPLICATION TO LAYERED MATERIALS

Trends in the Directional Dependence of κ_L . An anisotropic model for lattice thermal conductivity is of little use for materials which are known to be isotropic, such as cubic systems. The novelty of our model is best realized in materials which are likely to demonstrate anisotropic transport by breaking 3D symmetry. We have previously demonstrated that vdW- and ionic-layered materials demonstrate anisotropic elastic behavior. ⁶⁷

Here, we show the diversity of thermal transport within this group of materials. This set of layered materials is composed of binary and ternary vdW-layered (302 and 364 compounds, respectively) and ternary ionic-layered materials (1595 compounds) which we have previously identified. 1,66,67 The two classes of layered materials are differentiated by the nature of the interlayer bonding. In vdW-layered materials, the layers are weakly held together by vdW bonding, leading to large separations between layers. The layers can, however, be corrugated in ways which lead to highly nonplanar separations between the layers. Such corrugations can lead to nearly isotropic elastic behavior by either reducing the intralayer elastic response by limiting the transmission of longitudinal phonons or enhancing the interlayer coupling because of increased surface area. 67 Ionic-layered materials are defined by layers which are bound by either ionic or covalent bonds through a single "spacer" element. Ternary ioniclayered materials consist of binary layers with the third element acting as the interlayer spacer. Such materials can be identified by first removing the spacer element and utilizing an algorithm for identifying of vdW-layered materials on the resulting pseudobinary material. Ionic-layered materials occur most frequently when a large cation such as Ba or La sits between the binary layers; however, there are numerous examples in which anions such as oxygen can also act as spacer elements, typically leading to stronger interlayer bonding. vdW- and ionic-layered materials can demonstrate a high degree of elastic anisotropy, and the layering direction is not necessarily a predictor of the directional variance of elastic properties, leading to diverse and unexpected directional elastic behavior. 67 Because the lattice thermal conductivity stems in large part from elastic properties, it is also reasonable to assume that we will find a number of materials which demonstrate large variability in the thermal transport.

In Figure 5, we show the extent of anisotropy in κ_L for both sets of layered compounds (all data can be found in the Supporting Information). In this figure, we plot the range of anisotropic values (vertical line from min to max) against the isotropic value of κ_L for ionic (blue)- and vdW (orange)-layered materials. The two outer guidelines represent a factor of 3 different from the isotropic value on either side. The inner guidelines represent a total factor of 1.5 between $\kappa_{L,\text{min}}$ and $\kappa_{L,\text{max}}$ which is the limit of the model's ability to distinguish between isotropic and anisotropic values. In this figure, we see that larger ranges from $\kappa_{L,\text{min}}$ to $\kappa_{L,\text{max}}$ are possible at higher isotropic values (Figure 5a). The average of the ratio $\kappa_{L,\text{max}}/\kappa_{L,\text{min}}$ for the entire set of materials is 3.42. Looking at only those materials in

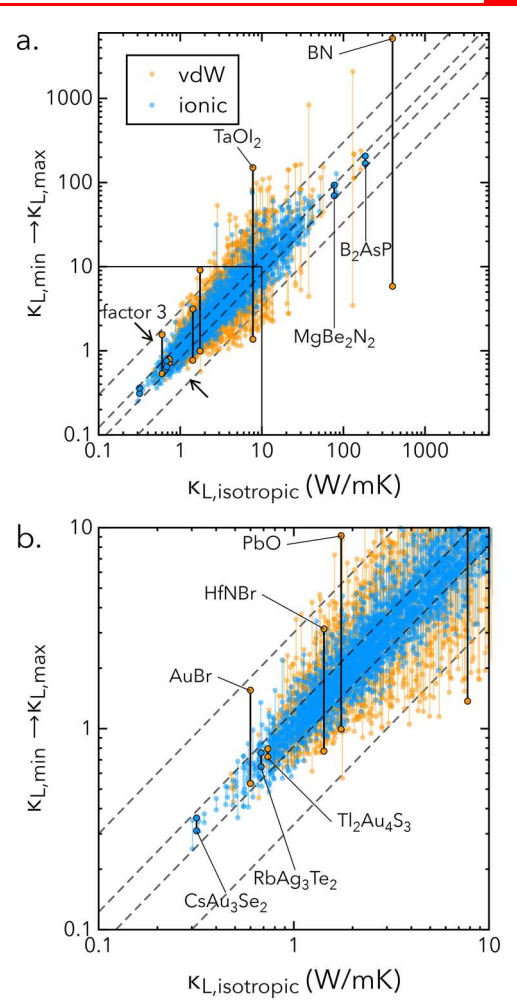


Figure 5. (a) Range of anisotropic κ_L from minimum to maximum values vs isotropic κ_L for ionic (blue)- and vdW (orange)-layered compounds. (b) Zoomed-in on lower isotropic values of κ_L . Case examples shown in Figures 7 and 8 are highlighted in black. Outer dashed lines indicate a factor of 3 different from the calculated isotropic value. Inner dashed lines represent a factor of 1.5 between $\kappa_{L, \min}$ and $\kappa_{L, \max}$.

the top 10% of $\kappa_{\rm L,iso}$, however, the average $\kappa_{\rm L,max}/\kappa_{\rm L,min}$ jumps to 11.89, over an order of magnitude of variation. For the lowest 10%, the average $\kappa_{\rm L,max}/\kappa_{\rm L,min}$ is only 1.50, which is nearly within the error of our model's predictive ability and therefore nearly indistinguishable from isotropic value. The narrowing of the range between $\kappa_{\rm L,min}$ and $\kappa_{\rm L,max}$ indicates that materials with low overall $\kappa_{\rm L}$ are approaching the amorphous limit (Figure 5b), which is the lowest value that $\kappa_{\rm L}$ can take for any material and is by definition isotropic. 20,30,80

Over the whole range, vdW-layered materials tend to demonstrate a larger directional variability in $\kappa_{\rm L}$ than ionic-layered materials. In Figure 6, we plot the distribution of anisotropy in $\kappa_{\rm L}$ for both sets of materials. We consider any material with $\kappa_{\rm L,max}/\kappa_{\rm L,min} < 1.5$ to be nearly isotropic because the average error in the slope of our model was 1.5. Over 60% of the ionic-layered materials meet this criteria, compared to less than 20% of the vdW-layered materials. Of the 666 vdW-layered compounds, 299 (45%) has a ratio of $\kappa_{\rm L,max}/\kappa_{\rm L,min} > 3$, with an overall average of $\kappa_{\rm L,max}/\kappa_{\rm L,min}$ equal to 7.60. With ionic-layered compounds, only 85 of 1595 (5.3%) have $\kappa_{\rm L,max}/\kappa_{\rm L,min} > 3$, with an overall average $\kappa_{\rm L,max}/\kappa_{\rm L,min}$ of 1.68. The fact that ionic-layered materials have lower $\kappa_{\rm L}$ anisotropy is consistent with the difference in the bonding anisotropy of these two sets, that is, layers in ionic-layered materials are more tightly bound than vdW-layered materials and therefore do not tend to demonstrate large differences between intralayer and interlayer bonding.

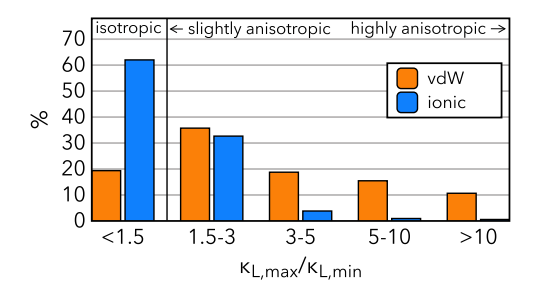


Figure 6. Histogram of anisotropy in κ_L for vdW (orange)- and ionic (blue)-layered materials. With the model accuracy, materials with $\kappa_{L,max}/\kappa_{L,min} < 1.5$ are essentially isotropic. Ionic-layered materials exhibit a much lower degree of anisotropy in κ_L than in vdW-layered materials, with over 60% falling into the isotropic region.

Layered Materials with Low κ_L . For very low values of κ_L (Figure 5b), we find that ionic-layered materials produce the lowest values, but that they are nearly isotropic (examples shown in Figure 7a-c). In contrast, anisotropic materials which have very low minimum values are typically vdW-layered materials (examples in Figure 7d-f). A common feature to the materials in Figure 7a-c is that the layers are either highly corrugated, leading to very low variation of κ_L between in-plane and out-of-plane directions. Figure 7a,b, CsAu₃Se₂ and RbAg₃Te₂, shows examples of ionic-layered materials with large cation spacer elements binding together the corrugated layers. Figure 7c shows Tl₂Au₄S₃, which is actually corrugated along two different in-plane directions. Tl₂Au₄S₃ could be classified either as vdW-layered materials because the Au-S bonds are significantly shorter than the Tl-S bonds or as ionic-layered materials with Tl acting as the spacer element. Layered materials with such isotropic transport are often where we find ambiguity in classification.

In Figure 7d–f, we show three examples of layered materials with low $\kappa_{L,min}$ which also demonstrates a large amount of anisotropy within κ_L . In Figure 7d, we show a very unique vdW-layered material, AuBr, which is a layered structure in which the layers are built from isolated and interwoven quasi-1D chains. The chains in each layer sit perpendicular to the chains in the neighboring layers, which is what allows this material to be classified as a quasi-2D structure because there is only one dividing plane. Because each layer is built from corrugated 1d chains, the in-plane κ_L is extremely low, 0.53 W/m K. The out-of-plane κ_L is actually the maximum in this example because the interlayer elastic coupling between crossed 1d chains is greater than the coupling between aligned chains within the same layer. Figure 7e,f shows two more typical examples (HfNBr and PbO) of vdW-layered materials in which the out-of-plane κ_L is very low because of the weak vdW bonding.

In the top half of Table 1, we list the 10 semiconductor materials with the lowest $\kappa_{\text{L,min}}$. Two things are immediately apparent from this list. The first is that the layered materials with lowest $\kappa_{\text{L,min}}$ are all very

Table 1. Top: Semiconductors with the Lowest $\kappa_{\rm L,min}$; Materials Are Sorted by Increasing $\kappa_{\rm L,min}$; Bottom: Semiconductor Materials with $\kappa_{\rm L,min} < 1~{\rm W/m~K~Which}$ Demonstrate Large Anisotropy in $\kappa_{\rm L}^{\rm a}$

compound	type	E_{g}	$K_{\mathrm{L,iso}}$	$\kappa_{ m L,min}$	$\kappa_{\rm L,max}$	$\kappa_{ m L,max}/\kappa_{ m L,min}$
$Cs_2Hg_3I_8$	ionic	1.8	0.30	0.25	0.35	1.39
CsAu ₃ S ₂	ionic	2.7	0.33	0.31	0.35	1.13
CsAu ₃ Se ₂	ionic	2.6	0.32	0.31	0.36	1.16
$RbAu_3Se_2$	ionic	2.2	0.35	0.34	0.38	1.11
$Cs_2Pt_3Se_4$	ionic	1.7	0.52	0.36	0.69	1.91
CsAu ₆ S ₅ *	ionic	2.7	0.40	0.39	0.45	1.14
$Cs_2Pt_3S_4$	ionic	2.1	0.58	0.41	0.84	2.07
Cs ₂ Pd ₃ Se ₄	ionic	1.4	0.55	0.41	0.73	1.78
Tl_4SnS_3	ionic	1.0	0.49	0.42	0.55	1.32
$CsAg_2I_3$	ionic	2.5	0.45	0.42	0.52	1.23
PbS*	vdW	0.8	1.77	0.57	8.72	15.40
PbO	vdW	1.3	1.75	0.99	9.13	9.17
ZrNI	vdW	1.2	2.25	0.90	6.87	7.59
TaTe₄I	vdW	0.4	1.03	0.72	3.50	4.84
ZrNBr	vdW	1.5	1.85	0.97	4.16	4.27
HfNCl	vdW	2.3	1.60	0.85	3.51	4.11
HfNBr	vdW	1.9	1.43	0.77	3.14	4.06
HfNI	vdW	1.0	1.39	0.77	2.96	3.84
ZrI_2	vdW	0.2	1.30	0.76	2.81	3.70
$Ta_{3}TeI_{7} \\$	vdW	0.5	1.39	0.82	2.72	3.31

^aMaterials are sorted by decreasing $\kappa_{\rm L,max}/\kappa_{\rm L,min}$. (* hypothetical structures). $E_{\rm g}$ in eV and $\kappa_{\rm L}$ in W/m K.

nearly isotropic, as evidenced by the last column of Table 1. This again confirms our understanding that as 3D bulk materials approach the lowest limit of κ_L (i.e., the amorphous limit), they tend to become more isotropic in their thermal transport, coinciding with the fact that an amorphous material must inherently be isotropic. The second feature that is apparent is the similar chemistry among layered materials with the lowest $\kappa_{L,min}$. These are all ionic-layered materials, and nearly all (except for Tl₄SnS₃) have a heavy, highly electropositive cation from group 1 (Cs or Rb), a heavy d-block metal from groups 10-12 (Hg, Au, Pt, and Pd), and a similarly electronegative anion (S, Se, and I). Of the known materials, ^{84–90} we find materials known for applications such as nonlinear optics $(Cs_2Hg_3I_8)$, ⁸⁴ optoelectronics (Tl_4SnS_3) , ⁸⁹ and superionic conductors $(CsAg_2I_3)$. ⁹⁰ In the lower half of Table 1, we list 10 semiconducting materials with $\kappa_{L,min}$ of 1 W/m K which also has anisotropic κ_L . These materials are all vdW-layered materials where $\kappa_{L,min}$ lies in the out-of-plane direction. Apart from PbO⁹¹ and a hypothetical version of PbS, all of the other materials listed are known halogen-containing materials. Five of these compounds are metal-nitride-halides, 22 two are telluride-iodides (TaTe₄I and Ta₃TeI₇), 93,94 and one is a binary metal iodide

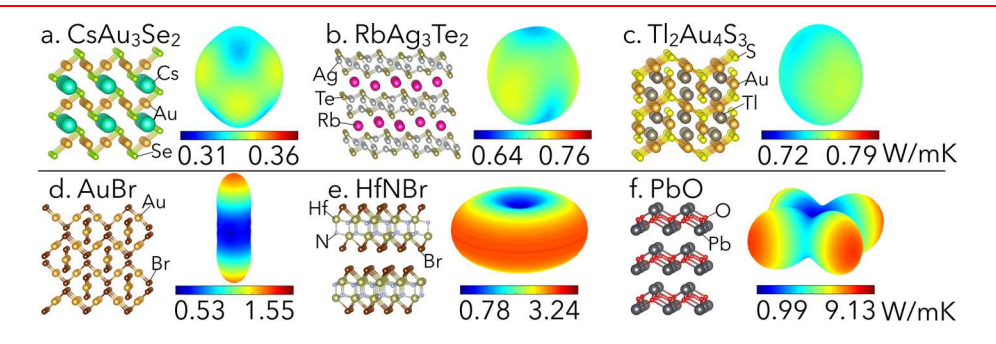


Figure 7. Case examples of layered materials with low minimum κ_L , ranging from nearly isotropic (a)–(c), to very anisotropic (d)–(f). For each material, the polar plot of κ_L is shown. The radius and color both represent the value of κ_L in W/m K. The minimum and maximum κ_L for each material are labeled next to the colorbar.

 (ZrI_2) . These anisotropic materials would be interesting candidates for anisotropic thermoelectrics if the out-of-plane mobility, either electron or hole, is reasonably large.

Layered Materials with High $\kappa_{\rm L,max}$. For high thermal conductivity, we focus on materials which have a maximum $\kappa_{\rm L}$ larger than 50 W/m K, where we find a total of 57 layered materials, 20 of which are ionic-layered materials and the other 37 are vdW-layered materials. Of the compounds with $\kappa_{\rm L,max} > 50$ W/m K, 32 of the 57 have $\kappa_{\rm L,max}/\kappa_{\rm L,min} > 5$, yet 12 have $\kappa_{\rm L,max}/\kappa_{\rm L,min} < 2$, confirming that not all layered materials with high $\kappa_{\rm L}$ are highly anisotropic. In Figure 8a–d, we highlight several case examples of materials with high thermal conductivity to illustrate various mechanisms by which high maximum $\kappa_{\rm L}$ can manifest.

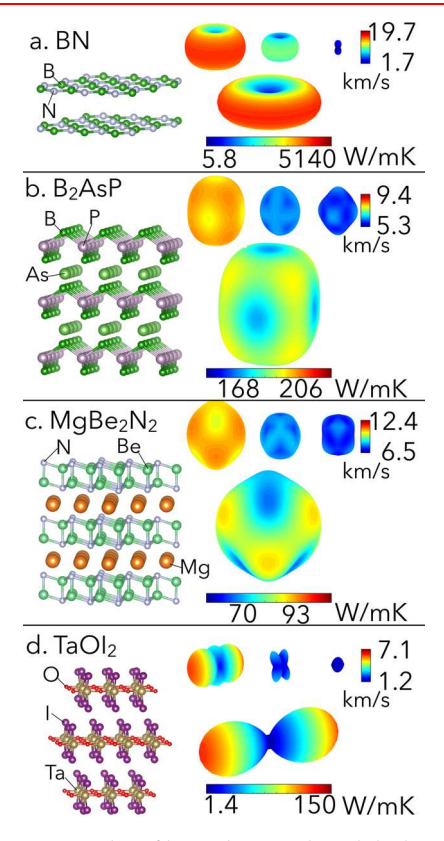


Figure 8. Case examples of layered materials with high maximum κ_L . For each material, the polar plots of speeds of sound (longitudinal and transverse) are shown in addition to the polar plot of κ_L (B₂AsP is a hypothetical material). For each polar plot, the radius and color both represent the value of the parameter. The minimum and maximum values of the parameter are labeled next to the colorbars.

Figure 8a shows hexagonal BN, one of the most common examples of a vdW-layered structure. $^{9,36,67,97-102}$ The extremely high in-plane $\kappa_{\rm L,max}$ is consistent with the order of magnitude of prior predicted values for hexagonal BN, which has been shown to have a theoretical value well over 1000 W/m K in the plane of the layers. 103 The ionic-layered compounds B₂AsP (theoretical) 96 and MgBe₂N₂ (Figure 8b,c) demonstrate high, nearly isotropic values for $\kappa_{\rm L}$, which stems from the tighter bonding inherent in this class of material. Figure 8d shows a unique vdW-layered ternary material, TaOI₂, which exhibits a quasi-1D thermal transport despite being a quasi-2D structure. The 1D transport stems from the asymmetry in the intralayer bonding.

Materials with high $\kappa_{\rm L}$ can potentially be candidates for power electronics. Apart from high thermal conductivity, power electronics require large band gaps above all else. 104,105 In Table 2, we list the top 10 materials with high $\kappa_{\rm L,max}$ and with DFT-calculated band gaps greater than 1 eV. Standard DFT calculations are known to underestimate band gaps, 106 which is why we choose to set the

Table 2. Candidate Semiconductor Materials for Single-Crystal High-Thermal-Transport Applications with High $\kappa_{\rm L,max}$ and $E_{\rm g} > 1~{\rm eV}^a$

compound	layer	E_{g}	$\kappa_{\mathrm{L,iso}}$	$\kappa_{ m L,min}$	$K_{L,max}$	$\kappa_{\rm L,max}/\kappa_{\rm L,min}$
BN_{hex}	vdW	4.2	399.9	5.8	5140.6	880.1
SnF_4	vdW	3.1	25.9	6.4	158.3	24.6
HfO_2	vdW	4.6	56.4	44.7	153.0	3.4
ZnSiO ₃ *	vdW	3.9	52.7	40.4	114.4	2.8
$MgBe_2N_2$	ionic	4.1	77.2	69.7	92.9	1.3
PbF_4	vdW	1.9	11.7	3.2	81.2	25.7
BiB_3O_6	ionic	3.9	7.6	4.5	76.6	17.1
Ba_2ZrO_4	ionic	3.0	50.8	45.3	68.1	1.5
$LiAlO_2$	ionic	6.1	33.5	23.3	65.0	2.8
WS_2	vdW	1.2	13.5	2.2	63.9	28.6

^aCompounds are sorted by decreasing $\kappa_{L,max}$ expressed in W/m K.

cutoff at 1 eV. Of the candidate materials listed, half has a variation in $\kappa_{\rm L}$ greater than an order of magnitude. These highly anisotropic candidates include two well-known materials (hexagonal BN and the transition metal dichalcogenide WS₂), ¹⁰⁷ two vdW-layered binary fluorides (SnF₄ and PbF₄), ¹⁰⁸ and the ionic-layered oxide BiB₃O₆ (a known nonlinear optical material). ¹⁰⁹ Apart from BN, all of these anisotropic materials have isotropic values less than 30 W/m K, meaning that they would only be appealing candidates for high thermal conductivity applications in which anisotropy is taken into account. Among the more isotropic compounds with high $\kappa_{\rm L}$, we find HfO₂ (used in high speed bipolar switching), ¹¹⁰ a hypothetical-layered ZnSiO₃, the nitridoberyllate MgBe₂N₂, ¹¹¹ the ionic-layered compound Ba₂ZrO₄, ¹¹² and a high-pressure phase of LiAlO₂. ¹¹³ These layered materials with high $\kappa_{\rm L}$ and low thermal anisotropy would be interesting candidates for applications of power electronics as bulk 3D crystals.

CONCLUSIONS

In this work, we have developed a new semiempirical model to predict the direction-dependent κ_L . The new model, which is an extension of our prior isotropic κ_L model, maintains the computationally tractability of its predecessor without sacrificing the prediction accuracy. This model can, therefore, be utilized for rapid prediction of anisotropic κ_L in highthroughput searches. The robustness of the model can be gauged from the fact that it performs well for both materials with isotropic κ_L as well as those with highly anisotropic κ_L . We have demonstrated the utility and computational tractability of the model in a large-scale study of the κ_{L} anisotropy of 2200 layered materials. Our findings challenge the perceived notion that layered materials generally exhibit highly anisotropic properties. Surprisingly, we find many vdW- and ionic-layered materials with nearly isotropic κ_L . Additionally, we have also revealed layered materials with a unique thermal-transport behavior, such as those with one-dimensional heat-transport channels. With this new model, we can now begin to rapidly assess and identify materials for single-crystal thermal applications, where anisotropy or the lack thereof is a key requirement.

METHODS

Structures of all of the materials are obtained from the ICSD.⁷⁹ We perform structural relaxation and calculation of the elastic tensor using the Vienna Ab-initio Simulation Package^{114,115} with projector-augmented waves.^{116,117} Ionic-layered materials were previously relaxed using the generalized gradient approximation with the Perdew–Burke–Ernzerhof¹¹⁸ exchange–correlation functional,⁶⁷ whereas vdW-layered materials were previously relaxed using a

vdW-corrected exchange correlation functional (optB86) to correctly account for the long-range vdW interactions. 1,66,119,120 A plane wave cutoff energy of 520 eV and a fairly dense Γ -centered k-point grid of 1000 per inverse atom was used. 121 Elastic stiffness tensors were calculated with a finite difference method, in which six finite distortions of the lattice are performed and the elastic constants (C_{ij}) are derived from the stress—strain relationship. 66,67,122,123 Calculations are handled within the Python-based, high-throughput framework, PyLada. 124 Theoretical materials, identified by a keyword search of the crystallographic information file (cif), are marked in the Supporting Information.

ASSOCIATED CONTENT

S Supporting Information

The Supporting Information is available free of charge on the ACS Publications website at DOI: 10.1021/acs.chemmater.8b05084.

Computed material properties of 2255 ionic- and vdW-layered compounds considered in this work; materials properties including crystallographic and elastic properties, and sound velocities and lattice thermal conductivities; and experimental data of compounds used in model validation (XLSX)

AUTHOR INFORMATION

Corresponding Author

*E-mail: vstevano@mines.edu.

ORCID ®

Robert McKinney: 0000-0003-3672-4345

Note:

The authors declare no competing financial interest.

ACKNOWLEDGMENTS

We acknowledge support from the National Science Foundation DMR program, grant no. 1729594, and the Research Corporation for Scientific Advancement via the Cottrell Scholar Award. The research was performed using computational resources sponsored by the Department of Energy's Office of Energy Efficiency and Renewable Energy and located at the National Renewable Energy Laboratory.

REFERENCES

- (1) Gorai, P.; Toberer, E. S.; Stevanović, V. Computational identification of promising thermoelectric materials among known quasi-2D binary compounds. *J. Mater. Chem. A* **2016**, *4*, 11110–11116.
- (2) Huang, S.; Liu, H. J.; Fan, D. D.; Jiang, P. H.; Liang, J. H.; Cao, G. H.; Liang, R. Z.; Shi, J. First-Principles Study of the Thermoelectric Properties of the Zintl Compound KSnSb. *J. Phys. Chem. C* **2018**, *122*, 4217–4223.
- (3) Seko, A.; Togo, A.; Hayashi, H.; Tsuda, K.; Chaput, L.; Tanaka, I. Prediction of Low-Thermal-Conductivity Compounds with First-Principles Anharmonic Lattice-Dynamics Calculations and Bayesian Optimization. *Phys. Rev. Lett.* **2015**, *115*, 205901.
- (4) Miller, S. A.; Gorai, P.; Ortiz, B. R.; Goyal, A.; Gao, D.; Barnett, S. A.; Mason, T. O.; Snyder, G. J.; Lv, Q.; Stevanović, V.; Toberer, E. S. Capturing Anharmonicity in a Lattice Thermal Conductivity Model for High-Throughput Predictions. *Chem. Mater.* **2017**, *29*, 2494–2501.
- (5) Zeier, W. G.; Zevalkink, A.; Gibbs, Z. M.; Hautier, G.; Kanatzidis, M. G.; Snyder, G. J. Thinking Like a Chemist: Intuition in Thermoelectric Materials. *Angew. Chem., Int. Ed.* **2016**, *55*, 6826–
- (6) Dow, H. S.; Kim, W. S.; Lee, J. W. Thermal and electrical properties of silicon nitride substrates. *AIP Adv.* **2017**, *7*, 095022.

(7) Chow, T. P.; Tyagi, R. Wide bandgap compound semi-conductors for superior high-voltage unipolar power devices. *IEEE Trans. Electron Devices* **1994**, *41*, 1481–1483.

- (8) Hudgins, J. L.; Simin, G. S.; Santi, E.; Khan, M. A. An assessment of wide bandgap semiconductors for power devices. *IEEE Trans. Power Electron.* **2003**, *18*, 907–914.
- (9) Lindsay, L.; Broido, D. A. Enhanced thermal conductivity and isotope effect in single-layer hexagonal boron nitride. *Phys. Rev. B* **2011**, *84*, 155421.
- (10) Carrete, J.; Li, W.; Mingo, N.; Wang, S.; Curtarolo, S. Finding Unprecedentedly Low-Thermal-Conductivity Half-Heusler Semiconductors via High-Throughput Materials Modeling. *Phys. Rev. X* **2014**, *4*, 011019.
- (11) Hicks, L. D.; Dresselhaus, M. S. Effect of quantum-well structures on the thermoelectric figure of merit. *Phys. Rev. B* **1993**, 47, 12727–12731.
- (12) Slack, G. A. Nonmetallic crystals with high thermal conductivity. *J. Phys. Chem. Solids* **1973**, 34, 321–335.
- (13) Balandin, A. A.; Ghosh, S.; Bao, W.; Calizo, I.; Teweldebrhan, D.; Miao, F.; Lau, C. N. Superior Thermal Conductivity of Single-Layer Graphene. *Nano Lett.* **2008**, *8*, 902–907.
- (14) Vineis, C. J.; Shakouri, A.; Majumdar, A.; Kanatzidis, M. G. Nanostructured Thermoelectrics: Big Efficiency Gains from Small Features. *Adv. Mater.* **2010**, *22*, 3970–3980.
- (15) Aronov, D.; Andalman, A. S.; Fee, M. S. A Specialized Forebrain Circuit for Vocal Babbling in the Juvenile Songbird. *Science* **2008**, *320*, *630*–*634*.
- (16) Horie, C.; Krumhansl, J. A. Boltzmann Equation in a Phonon System. *Phys. Rev.* **1964**, *136*, A1397–A1407.
- (17) Hardy, R. J. Phonon Boltzmann Equation and Second Sound in Solids. *Phys. Rev. B* **1970**, 2, 1193–1207.
- (18) Guyer, R. A.; Krumhansl, J. A. Solution of the Linearized Phonon Boltzmann Equation. *Phys. Rev.* **1966**, *148*, 766–778.
- (19) Li, W.; Carrete, J.; Katcho, N. A.; Mingo, N. S.B. T. E. ShengBTE: A solver of the Boltzmann transport equation for phonons. *Comput. Phys. Commun.* **2014**, *185*, 1747–1758.
- (20) Gorai, P.; Stevanović, V.; Toberer, E. S. Computationally guided discovery of thermoelectric materials. *Nat. Rev. Mater.* **2017**, *2*, 17053.
- (21) Broido, D. A.; Malorny, M.; Birner, G.; Mingo, N.; Stewart, D. A. Intrinsic lattice thermal conductivity of semiconductors from first principles. *Appl. Phys. Lett.* **2007**, *91*, 231922.
- (22) Ward, A.; Broido, D. A.; Stewart, D. A.; Deinzer, G. Ab initio theory of the lattice thermal conductivity in diamond. *Phys. Rev. B* **2009**, *80*, 125203.
- (23) Ward, A.; Broido, D. A. Intrinsic phonon relaxation times from first-principles studies of the thermal conductivities of Si and Ge. *Phys. Rev. B* **2010**, *81*, 085205.
- (24) Li, W.; Mingo, N.; Lindsay, L.; Broido, D. A.; Stewart, D. A.; Katcho, N. A. Thermal conductivity of diamond nanowires from first principles. *Phys. Rev. B* **2012**, *85*, 195436.
- (25) Li, W.; Mingo, N. Thermal conductivity of bulk and nanowire InAs, AlN, and BeO polymorphs from first principles. *J. Appl. Phys.* **2013**, *114*, 183505.
- (26) Zhao, L.-D.; Lo, S.-H.; Zhang, Y.; Sun, H.; Tan, G.; Uher, C.; Wolverton, C.; Dravid, V. P.; Kanatzidis, M. G. Ultralow thermal conductivity and high thermoelectric figure of merit in SnSe crystals. *Nature* **2014**, *508*, 373–377.
- (27) Shao, H.; Tan, X.; Liu, G.-Q.; Jiang, J.; Jiang, H. A first-principles study on the phonon transport in layered BiCuOSe. *Sci. Rep.* **2016**, *6*, 21035.
- (28) González-Romero, R. L.; Antonelli, A.; Chaves, A. S.; Meléndez, J. J. Ultralow and anisotropic thermal conductivity in semiconductor As 2 Se 3. *Phys. Chem. Chem. Phys.* **2018**, 20, 1809–1816.
- (29) Toher, C.; Plata, J. J.; Levy, O.; de Jong, M.; Asta, M.; Nardelli, M. B.; Curtarolo, S. High-throughput computational screening of thermal conductivity, Debye temperature, and Grüneisen parameter using a quasiharmonic Debye model. *Phys. Rev. B* **2014**, *90*, 174107.

(30) Yan, J.; Gorai, P.; Ortiz, B.; Miller, S.; Barnett, S. A.; Mason, T.; Stevanović, V.; Toberer, E. S. Material descriptors for predicting thermoelectric performance. *Energy Environ. Sci.* **2015**, *8*, 983–994.

- (31) Gorai, P.; Gao, D.; Ortiz, B.; Miller, S.; Barnett, S. A.; Mason, T.; Lv, Q.; Stevanović, V.; Toberer, E. S. TE Design Lab: A virtual laboratory for thermoelectric material design. *Comput. Mater. Sci.* **2016**, *112*, 368–376.
- (32) Madsen, G. K. H.; Katre, A.; Bera, C. Calculating the thermal conductivity of the silicon clathrates using the quasi-harmonic approximation. *Phys. Status Solidi A* **2016**, 213, 802–807.
- (33) Yan, X.; Poudel, B.; Ma, Y.; Liu, W. S.; Joshi, G.; Wang, H.; Lan, Y.; Wang, D.; Chen, G.; Ren, Z. F. Experimental Studies on Anisotropic Thermoelectric Properties and Structures of n-Type Bi2Te2.7Se0.3. *Nano Lett.* **2010**, *10*, 3373–3378.
- (34) Gibbs, Z. M.; Ricci, F.; Li, G.; Zhu, H.; Persson, K.; Ceder, G.; Hautier, G.; Jain, A.; Snyder, G. J. Effective mass and Fermi surface complexity factor from ab initio band structure calculations. *npj Comput. Mater.* **2017**, *3*, 8.
- (35) Novoselov, K. S.; Mishchenko, A.; Carvalho, A.; Castro Neto, A. H. 2D materials and van der Waals heterostructures. *Science* **2016**, 353, aac9439.
- (36) Kaul, A. B. Two-dimensional layered materials: Structure, properties, and prospects for device applications. *J. Mater. Res.* **2014**, 29, 348–361.
- (37) Qiao, J.; Kong, X.; Hu, Z.-X.; Yang, F.; Ji, W. High-mobility transport anisotropy and linear dichroism in few-layer black phosphorus. *Nat. Commun.* **2014**, *5*, 4475.
- (38) Miró, P.; Audiffred, M.; Heine, T. An atlas of two-dimensional materials. *Chem. Soc. Rev.* **2014**, *43*, 6537–6554.
- (39) Naguib, M.; Mochalin, V. N.; Barsoum, M. W.; Gogotsi, Y. 25th Anniversary Article: MXenes: A New Family of Two-Dimensional Materials. *Adv. Mater.* **2014**, *26*, 992–1005.
- (40) Rasmussen, F. A.; Thygesen, K. S. Computational 2D Materials Database: Electronic Structure of Transition-Metal Dichalcogenides and Oxides. *J. Phys. Chem. C* **2015**, *119*, 13169–13183.
- (41) Singh, A. K.; Mathew, K.; Zhuang, H. L.; Hennig, R. G. Computational Screening of 2D Materials for Photocatalysis. *J. Phys. Chem. Lett.* **2015**, *6*, 1087–1098.
- (42) Ashton, M.; Paul, J.; Sinnott, S. B.; Hennig, R. G. Topology-Scaling Identification of Layered Solids and Stable Exfoliated 2D Materials. *Phys. Rev. Lett.* **2017**, *118*, 106101.
- (43) Goldsmid, H. J. The Thermal Conductivity of Bismuth Telluride. *Proc. Phys. Soc., London, Sect. B* **1956**, *69*, 203–209.
- (44) Shaver, P. J.; Blair, J. Thermal and Electronic Transport Properties of p-Type ZnSb. *Phys. Rev.* **1966**, *141*, 649–663.
- (45) Spitzer, D. P. Lattice thermal conductivity of semiconductors: A chemical bond approach. *J. Phys. Chem. Solids* **1970**, *31*, 19–40.
- (46) Slack, G. A.; Austerman, S. B. Thermal Conductivity of BeO Single Crystals. J. Appl. Phys. 1971, 42, 4713–4717.
- (47) Slack, G. A. Thermal Conductivity of II-VI Compounds and Phonon Scattering by Fe²⁺ Impurities. *Phys. Rev. B* **1972**, *6*, 3791–3800.
- (48) Turkes, P.; Pluntke, C.; Helbig, R. Thermal conductivity of SnO2 single crystals. *J. Phys. C: Solid State Phys.* **1980**, 13, 4941–4951
- (49) Slack, G. A.; Tanzilli, R. A.; Pohl, R. O.; Vandersande, J. W. The intrinsic thermal conductivity of AIN. *J. Phys. Chem. Solids* **1987**, 48, 641–647.
- (50) Li, B.; Pottier, L.; Roger, J. P.; Fournier, D.; Watari, K.; Hirao, K. Measuring the anisotropic thermal diffusivity of silicon nitride grains by thermoreflectance microscopy. *J. Eur. Ceram. Soc.* **1999**, *19*, 1631–1639.
- (51) Liu, J.; Choi, G.-M.; Cahill, D. G. Measurement of the anisotropic thermal conductivity of molybdenum disulfide by the time-resolved magneto-optic Kerr effect. *J. Appl. Phys.* **2014**, *116*, 233107.
- (52) Kumar, S.; Schwingenschlögl, U. Lattice thermal conductivity in layered BiCuSeO. *Phys. Chem. Chem. Phys.* **2016**, *18*, 19158–19164.

(53) Gandi, A. N.; Schwingenschlögl, U. Thermal conductivity of bulk and monolayer MoS₂. EPL **2016**, 113, 36002.

- (54) Slack, G. A. Anisotropic Thermal Conductivity of Pyrolytic Graphite. *Phys. Rev.* **1962**, *127*, 694–701.
- (55) Alofi, A.; Srivastava, G. P. Thermal conductivity of graphene and graphite. *Phys. Rev. B* **2013**, *87*, 115421.
- (56) Pisoni, A.; Jacimovic, J.; Gaál, R.; Náfrádi, B.; Berger, H.; Révay, Z.; Forró, L. Anisotropic transport properties of tungsten disulfide. *Scr. Mater.* **2016**, *114*, 48–50.
- (57) Jiang, P.; Qian, X.; Gu, X.; Yang, R. Probing Anisotropic Thermal Conductivity of Transition Metal Dichalcogenides MX2 (M = Mo,W and X = S,Se) using Time-Domain Thermoreflectance. *Adv. Mater.* **2017**, 29, 1701068.
- (58) Carrete, J.; Mingo, N.; Curtarolo, S. Low thermal conductivity and triaxial phononic anisotropy of SnSe. *Appl. Phys. Lett.* **2014**, *105*, 101907.
- (59) Wei, P.-C.; Bhattacharya, S.; He, J.; Neeleshwar, S.; Podila, R.; Chen, Y. Y.; Rao, A. M. The intrinsic thermal conductivity of SnSe. *Nature* **2016**, *539*, E1–E2.
- (60) Klemens, P. G.; Pedraza, D. F. Thermal conductivity of graphite in the basal plane. *Carbon* **1994**, *32*, 735–741.
- (61) Chen, X.; Parker, D.; Singh, D. J. Acoustic impedance and interface phonon scattering in Bi₂Te₃ and other semiconducting materials. *Phys. Rev. B* **2013**, 87, 045317.
- (62) Jaeken, J. W.; Cottenier, S. Solving the Christoffel equation: Phase and group velocities. *Comput. Phys. Commun.* **2016**, 207, 445–451.
- (63) Epstein, S.; DeBretteville, A. P. Elastic Constants of and Wave Propagation in Antimony and Bismuth. *Phys. Rev.* **1965**, *138*, A771–A779.
- (64) Marmier, A.; Lethbridge, Z. A. D.; Walton, R. I.; Smith, C. W.; Parker, S. C.; Evans, K. E. ElAM: A computer program for the analysis and representation of anisotropic elastic properties. *Comput. Phys. Commun.* **2010**, *181*, 2102–2115.
- (65) Ranganathan, S. I.; Ostoja-Starzewski, M. Universal Elastic Anisotropy Index. *Phys. Rev. Lett.* **2008**, *101*, 055504.
- (66) Manna, S.; Gorai, P.; Brennecka, G. L.; Ciobanu, C. V.; Stevanović, V. Large piezoelectric response of van der Waals layered solids. *J. Mater. Chem. C* **2018**, *6*, 11035–11044.
- (67) McKinney, R. W.; Gorai, P.; Manna, S.; Toberer, E.; Stevanović, V. Ionic vs. van der Waals Layered Materials: Identification and Comparison of Elastic Anisotropy. *J. Mater. Chem. A* **2018**, *6*, 15828–15838.
- (68) Toberer, E. S.; Zevalkink, A.; Snyder, G. J. Phonon engineering through crystal chemistry. *J. Mater. Chem.* **2011**, *21*, 15843–15852.
- (69) Birch, F. Elasticity and constitution of the Earth's interior. *J. Geophys. Res.* **1952**, *57*, 227–286.
- (70) Mayer, W. G.; Parker, P. M. Method for the determination of elastic constants of trigonal crystal systems. *Acta Crystallogr.* **1961**, *14*, 725–726
- (71) Every, A. G. General closed-form expressions for acoustic waves in elastically anisotropic solids. *Phys. Rev. B* **1980**, *22*, 1746–1760.
- (72) Crampin, S. An introduction to wave propagation in anisotropic media. *Geophys. J. Int.* **1984**, *76*, 17–28.
- (73) Walker, A. M.; Wookey, J. MSATA new toolkit for the analysis of elastic and seismic anisotropy. *Comput. Geosci.* **2012**, *49*, 81–90.
- (74) Lane, C. The Development of a 2D Ultrasonic Array Inspection for Single Crystal Turbine Blades; Springer Science & Business Media: Heidelberg, 2014; Chapter 2, pp 13–39.
- (75) Jenkins, J. O.; Rayne, J. A.; Ure, R. W. Elastic Moduli and Phonon Properties of Bi₂Te₃. Phys. Rev. B 1972, 5, 3171–3184.
- (76) Feldman, J. L. Elastic constants of 2H-MoS2 and 2H-NbSe2 extracted from measured dispersion curves and linear compressibilities. *J. Phys. Chem. Solids* **1976**, *37*, 1141–1144.
- (77) Tsubouchi, K.; Sugai, K.; Mikoshiba, N. AlN Material Constants Evaluation and SAW Properties on AlN/AlO and AlN/Si. 1981 Ultrasonics Symposium, 1981; pp 375–380.

(78) del Corro, E.; de la Roza, A. O.; Taravillo, M.; Baonza, V. G. Raman modes and Grüneisen parameters of graphite under compressive biaxial stress. *Carbon* **2012**, *50*, 4600–4606.

- (79) Belsky, A.; Hellenbrandt, M.; Karen, V. L.; Luksch, P. New developments in the Inorganic Crystal Structure Database (ICSD): accessibility in support of materials research and design. *Acta Crystallogr., Sect. B: Struct. Sci.* **2002**, *58*, 364–369.
- (80) Cahill, D. G.; Watson, S. K.; Pohl, R. O. Lower limit to the thermal conductivity of disordered crystals. *Phys. Rev. B* **1992**, *46*, 6131–6140.
- (81) Zhang, X.; Zhang, Z.; Yao, S.; Chen, A.; Zhao, X.; Zhou, Z. An effective method to screen sodium-based layered materials for sodium ion batteries. *npj Comput. Mater.* **2018**, *4*, 13.
- (82) Sun, J.; Singh, D. J. Thermoelectric properties of AMg₂X₂, AZn₂Sb₂ (A = Ca,Sr,Ba; X = Sb,Bi), and Ba₂ZnX₂ (X = Sb,Bi) Zintl compounds. *J. Mater. Chem. A* **2017**, *5*, 8499–8509.
- (83) Aykol, M.; Kim, S.; Wolverton, C. van der Waals Interactions in Layered Lithium Cobalt Oxides. *J. Phys. Chem. C* **2015**, *119*, 19053–19058.
- (84) Zhang, G.; Qin, J.; Liu, T.; Zhu, T.; Fu, P.; Wu, Y.; Chen, C. Synthesis, Characterization, and Crystal Growth of Cs₂Hg₃I₈: A New Second-Order Nonlinear Optical Material. *Cryst. Growth Des.* **2008**, *8*, 2946–2949.
- (85) Klepp, K. O.; Weithaler, C. The crystal structures of CsAu₃S₂, RbAu₃Se₂ and CsAu₃Se₂ and their relationship to the CsCu₃S₂ structure type. *J. Alloys Compd.* **1996**, 243, 1–5.
- (86) Huster, J.; Bronger, W. Zur Struktur der Selenide Cs2Pd3Se4, Rb2Pd3Se4 und K₂Pd₃Se₄/On the Crystal Structure of Cs₂Pd₃Se₄, Rb₂Pd₃Se₄, and K₂Pd₃Se₄. Z. Naturforsch., B: J. Chem. Sci. 1974, 29, 594–595.
- (87) Günther, O.; Bronger, W. Cs₂Pt₃S₄ und Rb₂Pt₃S₄, synthese und struktur. *I. Less-Common Met.* **1973**, 31, 255–262.
- (88) Bronger, W.; Rennau, R. M.; Schmitz, D. Darstellung und Kristallstruktur von Rb2Ni3Se4. Z. Anorg. Allg. Chem. 1996, 622, 627–629.
- (89) Barchij, I.; Sabov, M.; El-Naggar, A. M.; AlZayed, N. S.; Albassam, A. A.; Fedorchuk, A. O.; Kityk, I. V. Tl₄SnS₃, Tl₂4SnSe₃ and Tl₄SnTe₃ crystals as novel IR induced optoelectronic materials. *J. Mater. Sci.: Mater. Electron.* **2016**, *27*, 3901–3905.
- (90) Rafiuddin; Hassan, M. A superionic conducting phase in Cd-substituted CsAg₂I₃. *Solid State Commun.* **2007**, 144, 293–295.
- (91) Leciejewicz, J. On the crystal structure of tetragonal (red) PbO. *Acta Crystallogr.* **1961**, *14*, 1304.
- (92) Chen, X.; Koiwasaki, T.; Yamanaka, S. High-pressure synthesis and crystal structures of -MNX(M Zr, Hf;X Cl, Br, I). *J. Phys.: Condens. Matter* **2002**, *14*, 11209–11212.
- (93) Tremel, W. NbTe₄I und TaTe₄I, zwei neue Tellurid-Iodide mit Kettenstruktur. *Chem. Ber.* **1992**, *125*, 2165–2170.
- (94) Smith, M. D.; Miller, G. J. Tantalum-Niobium Mixing in $Ta_{3-x}Nb_xTeI_7$ (0 x 3). Z. Anorg. Allg. Chem. **2000**, 626, 94–102.
- (95) Guthrie, D. H.; Corbett, J. D. Synthesis and structure of an infinite-chain form of ZrI_2 (α). J. Solid State Chem. 1981, 37, 256–263.
- (96) Merabet, M.; Rached, D.; Khenata, R.; Benalia, S.; Abidri, B.; Bettahar, N.; Bin Omran, S. Electronic structure of (BP)n/(BAs)n (001) superlattices. *Phys. B* **2011**, *406*, 3247–3255.
- (97) Sichel, E. K.; Miller, R. E.; Abrahams, M. S.; Buiocchi, C. J. Heat capacity and thermal conductivity of hexagonal pyrolytic boron nitride. *Phys. Rev. B* **1976**, *13*, 4607–4611.
- (98) Novoselov, K. S.; Jiang, D.; Schedin, F.; Booth, T. J.; Khotkevich, V. V.; Morozov, S. V.; Geim, A. K. Two-dimensional atomic crystals. *Proc. Natl. Acad. Sci. U.S.A.* **2005**, *102*, 10451–10453.
- (99) Bosak, A.; Serrano, J.; Krisch, M.; Watanabe, K.; Taniguchi, T.; Kanda, H. Elasticity of hexagonal boron nitride: Inelastic x-ray scattering measurements. *Phys. Rev. B* **2006**, *73*, 041402.
- (100) Abdullaev, N. A. Elastic properties of layered crystals. *Phys. Solid State* **2006**, 48, 663–669.
- (101) Bruzzone, S.; Fiori, G. Ab-initio simulations of deformation potentials and electron mobility in chemically modified graphene and

two-dimensional hexagonal boron-nitride. Appl. Phys. Lett. 2011, 99, 222108.

- (102) Jo, I.; Pettes, M. T.; Kim, J.; Watanabe, K.; Taniguchi, T.; Yao, Z.; Shi, L. Thermal Conductivity and Phonon Transport in Suspended Few-Layer Hexagonal Boron Nitride. *Nano Lett.* **2013**, 13, 550–554.
- (103) Kelly, B. T. The thermal conductivity of hexagonal boron nitride parallel to the basal planes. *J. Nucl. Mater.* **1977**, *68*, 9–12.
- (104) Lebedev, A. A.; Chelnokov, V. E. Wide-gap semiconductors for high-power electronics. *Semiconductors* **1999**, 33, 999–1001.
- (105) Kaplar, R. J.; Neely, J. C.; Huber, D. L.; Rashkin, L. J. Generation-After-Next Power Electronics: Ultrawide-bandgap devices, high-temperature packaging, and magnetic nanocomposite materials. *IEEE Power Electronics Magazine* 2017, 4, 36–42.
- (106) Perdew, J. P. Density functional theory and the band gap problem. *Int. J. Quantum Chem.* **2009**, 28, 497–523.
- (107) Zhao, W.; Ghorannevis, Z.; Chu, L.; Toh, M.; Kloc, C.; Tan, P.-H.; Eda, G. Evolution of Electronic Structure in Atomically Thin Sheets of WS₂ and WSe₂. ACS Nano 2013, 7, 791–797.
- (108) Hoppe, R.; Dähne, W. Die Kristalistruktur von SnF₄ und PbF₄. Naturwissenschaften **1962**, 49, 254–255.
- (109) Hellwig, H.; Liebertz, J.; Bohatý, L. Exceptional large nonlinear optical coefficients in the monoclinic bismuth borate BiB3O6 (BIBO). *Solid State Commun.* **1998**, *109*, 249–251.
- (110) Lee, H. Y.; Chen, P. S.; Wu, T. Y.; Chen, Y. S.; Wang, C. C.; Tzeng, P. J.; Lin, C. H.; Chen, F.; Lien, C. H.; Tsai, M.-J. Low power and high speed bipolar switching with a thin reactive Ti buffer layer in robust HfO₂ based RRAM. 2008 IEEE International Electron Devices Meeting, 2008; pp 1–4.
- (111) Strobel, P.; Weiler, V.; Schmidt, P. J.; Schnick, W. $Sr[BeSi_2N_4]$: Eu^{2+}/Ce^{3+} and $Eu[BeSi_2N_4]$: Nontypical Luminescence in Highly Condensed Nitridoberyllosilicates. *Chem.—Eur. J.* **2018**, 24, 7243–7249.
- (112) Dash, S.; Singh, Z.; Prasad, R.; Sood, D. D. The determination of the standard molar Gibbs free energy of formation of Ba2ZrO4(s). *J. Chem. Thermodyn.* **1994**, *26*, 745–750.
- (113) Li, X.; Kobayashi, T.; Zhang, F.; Kimoto, K.; Sekine, T. A new high-pressure phase of LiAlO₂. *J. Solid State Chem.* **2004**, *177*, 1939–1943
- (114) Kresse, G.; Furthmüller, J. Efficiency of ab-initio total energy calculations for metals and semiconductors using a plane-wave basis set. *Comput. Mater. Sci.* **1996**, *6*, 15–50.
- (115) Kresse, G.; Furthmüller, J. Efficient iterative schemes forab initiototal-energy calculations using a plane-wave basis set. *Phys. Rev.* B **1996**, *54*, 11169–11186.
- (116) Blöchl, P. E. Projector augmented-wave method. *Phys. Rev. B* **1994**, *50*, 17953–17979.
- (117) Kresse, G.; Joubert, D. From ultrasoft pseudopotentials to the projector augmented-wave method. *Phys. Rev. B* **1999**, *59*, 1758–1775
- (118) Perdew, J. P.; Burke, K.; Ernzerhof, M. Generalized Gradient Approximation Made Simple. *Phys. Rev. Lett.* **1996**, *77*, 3865–3868.
- (119) Klimeš, J.; Bowler, D. R.; Michaelides, A. Van der Waals density functionals applied to solids. *Phys. Rev. B* **2011**, 83, 195131.
- (120) Wei, Y.; Yang, R. Nanomechanics of graphene. *Natl. Sci. Rev.* 2018, nwy067.
- (121) Monkhorst, H. J.; Pack, J. D. Special points for Brillouin-zone integrations. *Phys. Rev. B* **1976**, *13*, 5188–5192.
- (122) Le Page, Y.; Saxe, P. Symmetry-general least-squares extraction of elastic data for strained materials from *ab initio* calculations of stress. *Phys. Rev. B* **2002**, *65*, 104104.
- (123) Wu, X.; Vanderbilt, D.; Hamann, D. R. Systematic treatment of displacements, strains, and electric fields in density-functional perturbation theory. *Phys. Rev. B* **2005**, *72*, 035105.
- (124) Pylada: A Python framework for high-throughput first-principles calculations. 2013. https://github.com/pylada.